A One-dimensional Time Dependent Cloud Model

Shu-Hua CHEN

National Center for Atmospheric Research, Boulder, CO, USA

and

Wen-Yih SUN

Department of Earth and Atmospheric Sciences, Purdue University, West Lafayette, IN, USA

(Manuscript received 6 November 2000, in revised form 22 October 2001)

Abstract

A one-dimensional prognostic cloud model has been developed for possible use in a Cumulus Parameterization Scheme (CPS). In this model, the nonhydrostatic pressure, entrainment, cloud microphysics, lateral eddy mixing and vertical eddy mixing are included, and their effects are discussed.

The inclusion of the nonhydrostatic pressure can (1) weaken vertical velocities, (2) help the cloud develop sooner, (3) help maintain a longer mature stage, (4) produce a stronger overshooting cooling, and (5) approximately double the precipitation amount. The pressure perturbation consists of buoyancy pressure and dynamic pressure, and the simulation results show that both of them are important.

We have compared our simulation results with those from Ogura and Takahashi's one-dimensional cloud model, and those from the three-dimensional Weather Research and Forecast (WRF) model. Our model, including detailed cloud microphysics, generates stronger maximum vertical velocity than Ogura and Takahashi's results. Furthermore, the results illustrate that this one-dimensional model is capable of reproducing the major features of a convective cloud that are produced by the three-dimensional model when there is no ambient wind shear.

1. Introduction

Because of the significant influence of moist convection on mesoscale or synoptic weather phenomena, Kuo (1974), Arakawa and Schubert (1974), Fritsch and Chappell (1980), Betts (1986), Grell (1993), Sun and Haines (1996), and many others have proposed different Cumulus Parameterization Schemes (CPSs) to represent the sub-grid scale convection in a numerical model. A one-dimensional cloud model incorporated into CPSs can play an important role in the vertical mass flux, heating profile, drying profile, and precipitation rate. Kain and

Fritsch (1990) introduced a one-dimensional entraining/detraining plume model to improve the Fritsch-Chappell cumulus parameterization. They assumed that any mixture resulting in negative buoyancy detrains from the cloud, while other mixtures resulting in positive buoyancy entrain into the cloud. The conversion of condensate to precipitation and the cloud glaciation parameterized in their model were simplified. For the past few years, we have worked on a diagnostic one-dimensional cloud model (Haines and Sun 1994) and a new cumulus parameterization (Sun and Haines 1996), which can be incorporated into the Purdue Mesoscale Model (Haines 1992; Sun and Chern 1993; Chern 1994) to study convection and severe weather. However, the resolution of mesoscale models has been increasing, and a time dependent one-dimensional cloud model becomes required. Therefore, this paper presents our

Corresponding author and present affiliation: Shu-Hua Chen, Department of Land, Air, and Water Resources, University of California, Davis, CA 95616 USA.
E-mail: shachen@ucdavis.edu

continuous effort to develop a prognostic one-dimensional cloud model such that it can not only produce a realistic result, but also is simple enough to be incorporated into CPSs.

The effect of the nonhydrostatic pressure (pressure perturbation) on cloud development has been studied by Holton (1973), Schlesinger (1978), Yau (1979), Kuo and Raymond (1980). It is also well known that cloud microphysics plays an important role in the cloud's development and its precipitation. In Levi and Saluzzi (1996), the effect of ice formation on convective cloud development was discussed in detail. When the atmosphere is moderately unstable, the modifications of the freezing process in middle levels could remarkably influence the cloud development. However, this influence is not significant when the atmosphere is in a pronounced unstable condition.

So far, only a few one-dimensional cloud models have included more complete processes. Ferrier and Houze (1989) developed a quite sophisticated one-dimensional cloud model, which included pressure gradient force, cloud physics, entrainment, and vertical diffusion. However, only warm rain processes were counted in the microphysics since their model was applied to tropical studies. In Cheng (1989a), the entrainment/detainment was taken care in great detail, but the nonhydrostatic pressure was excluded, and only warm rain was considered. In addition, his model is a diagnostic cumulus ensemble model, which is more suitable for the cumulus parameterization scheme used in coarse resolution models. In our model, nonhydrostatic pressure, microphysics, entrainment, lateral eddy mixing, and vertical eddy mixing are all included. In particular, a more sophisticated microphysics is implemented.

A comparison between the one-dimensional cloud model and a three-dimensional cloud model will be very interesting and helpful. From this comparison, we can learn the capabilities and deficiencies of the one-dimensional cloud model, and then use this information to further improve the cumulus parameterization. The three-dimensional Weather Research and Forecast (WRF) model (Michalakes et al. 2001; Skamarock et al. 2001), which can be used as a cloud model or mesoscale model, is adopted for comparison. A comparison with observational data, such as radar data, will certainly be in-teresting, but we leave it for future work. It is also noted that more work should be done in the future to include the vertical wind shear and downdraft in this one-dimensional cloud model.

Section 2 describes the governing equations and numerical methods used in this one-dimensional cloud model. Section 3 presents a comparison of results between this model and another one-dimensional cloud model (Ogura and Takahashi 1971), and the importance of microphysics and nonhydrostatic pressure is discussed. Section 4 gives a brief introduction of the three-dimensional WRF model and a comparison between these two models' results. The forcing terms of vertical eddy mixing, lateral eddy mixing, entrainment, and microphysics in the one-dimensional model are also discussed. A brief summary is given in Section 5.

2. Model descriptions

2.1 Governing equations

The one-dimensional axi-symmetric cumulus cloud is assumed to be a function of t, r, ψ, and z, where t is time; r is radius; ψ is tangential angle; and z is height. The radius of the cloud can not only change with height (Ferrier and Houze 1989; Levi and Saluzzi 1996), but also changes with time. However, to simplify the problem, the radius is fixed once it is determined in our model. Coriolis force is ignored because of a small length scale ($\sim$ a few kilometers) and a short time scale ($\sim$ one hour). Molecular diffusion is also negligible compared with eddy turbulence diffusion. In a strong convective cumulus cloud, hydrostatic balance can no longer be held inside the cloud. Thus, the hypotheses of nonhydrostatic balance within the cloud and hydrostatic balance in the surrounding area are proposed. The governing equations of this cloud model are:

(i) Vertical momentum equation

$$\frac{\partial w}{\partial t} = -\frac{1}{r}\frac{\partial(urw)}{\partial r} - \frac{1}{r}\frac{\partial(vw)}{\partial \psi}$$
$$-\frac{1}{\rho_0}\frac{\partial(\rho_0 w^2)}{\partial z} - \frac{1}{\rho_0}\frac{\partial p_{nh}}{\partial z} + g\frac{(\theta_v - \theta_{v0})}{\theta_{v0}}$$
$$+ g\left(\frac{R}{C_p} - 1\right)\frac{p_{nh}}{p_0} - gQ_T, \tag{1}$$

where u, v, w, p_{nh}, θ_v, ρ_0, R, and C_p are radial

velocity, tangential velocity, vertical velocity, nonhydrostatic pressure, virtual potential temperature, surrounding density, gas constant for dry air, and specific heat of air at constant pressure. Q_T is total precipitation, and $-gQ_T$ is the drag force due to the weight of precipitation. Subscript zero ($_0$) indicates environmental values. The total pressure (p) within the cloud is split into the nonhydrostatic perturbation part (p_{nh}) and hydrostatic part (environment pressure, p_0), and

$$\frac{1}{\rho_0}\frac{\partial p_0}{\partial z} = -g.$$

(ii) Divergence equation

$$\frac{\partial \delta}{\partial t} = -\frac{1}{r}\frac{\partial(ur\delta)}{\partial r} - \frac{1}{r}\frac{\partial v\delta}{\partial \psi} - \frac{1}{\rho_0}\frac{\partial(\rho_0 w\delta)}{\partial z} - \delta^2$$
$$-\frac{\partial w}{\partial r}\frac{\partial u}{\partial z} - \frac{1}{r}\frac{\partial w}{\partial \psi}\frac{\partial v}{\partial z} + \frac{2}{r}\frac{\partial u}{\partial r}\frac{\partial v}{\partial \psi} - \frac{2}{r}\frac{\partial v}{\partial r}\frac{\partial u}{\partial \psi}$$
$$+\frac{1}{r}\frac{\partial u^2}{\partial r} + \frac{1}{r}\frac{\partial v^2}{\partial r} - \frac{1}{r}\frac{\partial}{\partial r}\left(\frac{r}{\rho_0}\frac{\partial p_{nh}}{\partial r}\right)$$
$$-\frac{1}{r}\frac{\partial}{\partial \psi}\left(\frac{1}{\rho_0 r}\frac{\partial p_{nh}}{\partial \psi}\right), \qquad (2)$$

where δ is horizontal divergence and its formula is:

$$\delta = \frac{1}{r}\frac{\partial(ur)}{\partial r} + \frac{1}{r}\frac{\partial v}{\partial \psi}.$$

(iii) Thermodynamic equation

$$\frac{\partial \theta_{ei}}{\partial t} = -\frac{1}{r}\frac{\partial(ur\theta_{ei})}{\partial r} - \frac{1}{r}\frac{\partial(v\theta_{ei})}{\partial \psi} - \frac{1}{\rho_0}\frac{\partial(\rho_0 w\theta_{ei})}{\partial z}$$
$$+\underbrace{\frac{1}{C_p}(L_v q_v - L_f q_i)\frac{d}{dt}\left(\frac{\theta}{T}\right)}_{(1)}$$
$$+\underbrace{micro(\theta_{ei})}_{(2)}, \qquad (3)$$

where q_v and q_i are the mixing ratios of water vapor and cloud ice, respectively. θ_{ei} is called equivalent ice potential temperature (Chern 1994) and it is defined as

$$\theta_{ei} = \theta\left[1 + \left(\frac{L_v q_v}{C_p T} - \frac{L_f q_i}{C_p T}\right)\right].$$

L_v, L_f and T are the latent heat of vaporization and fusion, and temperature within the cloud,

respectively. The derivation of this equation is similar to that using the equivalent potential temperature, but with the consideration of ice crystals. The equivalent ice potential temperature is approximately conserved if there is no rain, snow, and graupel falling out of air parcel and therefore, it has a better conservative property than the equivalent potential temperature. In the thermodynamic equation, term (1) is due to the change of θ/T following an air parcel and term (2) is the contribution from cloud microphysical processes. Because the equivalent ice potential temperature is a function of water vapor and cloud ice, the change of θ_{ei} needs to account for the phase change between vapor/liquid and snow/graupel and for the particle transformation between ice and snow/graupel, namely to account for the changes of snow and graupel. Therefore, the formula for term (2) is:

$$micro(\theta_{ei}) = \frac{\theta L_f}{C_p T}(P_s + P_g),$$

where P_s and P_g are equivalent to microphysical production terms of snow and graupel, respectively (the last term on the right-hand side of equation (6)).

(iv) Continuity equation

$$\frac{1}{r}\frac{\partial(ur)}{\partial r} + \frac{1}{r}\frac{\partial v}{\partial \psi} + \frac{1}{\rho_0}\frac{\partial(\rho_0 w)}{\partial z} = 0. \qquad (4)$$

Density ρ_0 is assumed only to be a function of height.

(v) Six equations of water substance

$$\frac{\partial q_x}{\partial t} = -\frac{1}{r}\frac{\partial(urq_x)}{\partial r} - \frac{1}{r}\frac{\partial(vq_x)}{\partial \psi}$$
$$-\frac{1}{\rho_0}\frac{\partial(\rho_0 wq_x)}{\partial z} + P_x, \qquad (5)$$
$$\frac{\partial q_y}{\partial t} = -\frac{1}{r}\frac{\partial(urq_y)}{\partial r} - \frac{1}{r}\frac{\partial(vq_y)}{\partial \psi} - \frac{1}{\rho_0}\frac{\partial(\rho_0 wq_y)}{\partial z}$$
$$+\frac{1}{\rho_0}\frac{\partial(\rho_0 V_{ty}q_y)}{\partial z} + P_y, \qquad (6)$$

where q_x is the mixing ratio of cloud water (q_c), cloud ice, or non-precipitable water (q_w), which is defined as $q_v + q_c + q_i$, and q_y is the mixing ratio of rain (q_r), snow (q_s), or graupel (q_g). V_{ty} is the terminal velocity of precipitation (rain,

snow or graupel). P_x and P_y are the microphysical production terms of q_x and q_y.

According to Asai and Kasahara (1967), we also define

(a) the horizontal area-average value within the cloud

$$\bar{A} = \frac{1}{\pi R^2} \int_0^{2\pi} \int_0^R A r \, dr \, d\psi,$$

where A is any cloud variable and R is the cloud radius.

(b) the deviation value from the horizontal average of the cloud

$$A' = A - \bar{A}.$$

(c) the lateral boundary average value of the cloud

$$\tilde{A}(R) = \frac{1}{2\pi} \int_0^{2\pi} A \, d\psi.$$

(d) the deviation value from the lateral boundary average of the cloud

$$A'' = A - \tilde{A}.$$

Similar to Holton (1973), we assume that the nonhydrostatic pressure can be expressed as $p_{nh}(r, z) = p^*(z) \times J_0(r)$, where $J_0(r)$ is the zeroth order of the first kind Bessel function. The radius of the cloud (R) satisfies the first root of $J_0(x) = 0$, where $x = \frac{\alpha}{R} \cdot r$ and $\alpha = 2.4048$. It is noted that the lateral nonhydrostatic pressure perturbation (p_{nh}) is zero under this assumption.

After horizontal averaging (see Appendix A), equations (1) to (6) become:

$$\frac{\partial \overline{w}}{\partial t} = -\frac{2}{R}(\tilde{u}\tilde{w} + \widetilde{u''w''}) - \frac{1}{\rho_0} \frac{\partial[\rho_0(\overline{w}\overline{w} + \overline{w'w'})]}{\partial z}$$
$$- \frac{2J_1(\alpha)}{\rho_0 \alpha} \frac{\partial p^*(z)}{\partial z} + g\left[\frac{\overline{\theta}_v - \theta_{v0}}{\theta_{v0}} - \overline{Q}_T\right.$$
$$\left. + \left(\frac{R}{C_p} - 1\right)\frac{2J_1(\alpha)}{\alpha}\frac{p^*(z)}{p_0}\right], \qquad (7)$$

$$\frac{\partial \overline{\delta}}{\partial t} = -\frac{2}{R}(\tilde{u}\tilde{\delta} + \widetilde{u''\delta''}) - \frac{1}{\rho_0} \frac{\partial[\rho_0(\overline{w}\overline{\delta} + \overline{w'\delta'})]}{\partial z}$$
$$- \frac{\overline{\delta}^2}{2} + \frac{\overline{\zeta}^2}{2} + \frac{2\alpha}{\rho_0 R^2} J_1(\alpha) p^*(z), \qquad (8)$$

$$\frac{\partial \overline{\theta}_{ei}}{\partial t} = -\frac{2}{R}(\tilde{u}\tilde{\theta}_{ei} + \widetilde{u''\theta''_{ei}}) - \frac{1}{\rho_0} \frac{\partial[\rho_0(\overline{w}\overline{\theta}_{ei} + \overline{w'\theta'_{ei}})]}{\partial z}$$
$$+ \frac{1}{C_p}(L_v \bar{q}_v - L_f \bar{q}_i) \frac{d}{dt}\left(\frac{\overline{\theta}}{\overline{T}}\right)$$
$$+ micro(\bar{\theta}_{ei}), \qquad (9)$$

$$\frac{2}{R}\tilde{u} + \frac{1}{\rho_0}\frac{\partial(\rho_0 \overline{w})}{\partial z} = 0, \qquad (10)$$

$$\frac{\partial \bar{q}_x}{\partial t} = -\frac{2}{R}(\tilde{u}\tilde{q}_x + \widetilde{u''q''_x})$$
$$- \frac{1}{\rho_0} \frac{\partial[\rho_0(\overline{w}\bar{q}_x + \overline{w'q'_x})]}{\partial z} + \bar{P}_x, \qquad (11)$$

and

$$\frac{\partial \bar{q}_y}{\partial t} = -\frac{2}{R}(\tilde{u}\tilde{q}_y + \widetilde{u''q''_y}) - \frac{1}{\rho_0} \frac{\partial[\rho_0(\overline{w}\bar{q}_y + \overline{w'q'_y})]}{\partial z}$$
$$+ \frac{1}{\rho_0}\frac{\partial(\rho_0 \overline{V}_{ty}\bar{q}_y)}{\partial z} + \bar{P}_y, \qquad (12)$$

where J_1 is the first order of the first kind Bessel function. $\overline{\zeta}$ is horizontal average of vorticity, and it is assumed zero. For any quantity A, $\tilde{u}\tilde{A}$, $\widetilde{u''A''}$, $(\partial/\partial z)(\overline{w}\overline{A})$, and $(\partial/\partial z)(\overline{w'A'})$ are termed entrainment, lateral eddy diffusion, vertical flux, and vertical eddy diffusion, respectively. The second order perturbation terms of $(\overline{\delta'\delta'})$, $(\overline{\delta'\zeta'})$, and $(\overline{V'_{ty}q'_y})$, and the one from term (1) in equation (3) are ignored. As in Holton (1973), the tilting terms are also ignored.

The continuity equation can be expressed in terms of the divergence field and vertical velocity field as:

$$\bar{\delta} + \frac{1}{\rho_0}\frac{\partial(\rho_0 \overline{w})}{\partial z} = 0, \qquad (13)$$

Combining $\rho_0 \times (7) + (\partial/\partial z)[\rho_0 \times (8)]$ with the continuity equation (13), we can obtain the diagnostic equation for pressure perturbation (p^*), which is divided into a buoyancy part (p_b^*) and a dynamic part (p_d^*). Thus,

$$p^* = p_b^* + p_d^*, \qquad (14)$$

$$\frac{2J_1}{\alpha} \times \frac{\partial^2 p_b^*(z)}{\partial z^2} - \left(\frac{R}{C_p} - 1\right)g\frac{2J_1}{\alpha}\frac{\partial}{\partial z}\left(\rho_0 \frac{p_b^*(z)}{p_0}\right)$$
$$- \frac{2\alpha}{R^2}J_1 p_b^*(z)$$
$$= g\frac{\partial}{\partial z}\left(\rho_0 \frac{\overline{\theta}_v - \theta_{v0}}{\theta_{v0}}\right) - g\frac{\partial}{\partial z}(\rho_0 \overline{Q}_T), \qquad (15)$$

and

$$\frac{2J_1}{\alpha} \times \frac{\partial^2 p_d^*(z)}{\partial z^2} - \left(\frac{R}{C_p} - 1\right) g \frac{2J_1}{\alpha} \frac{\partial}{\partial z}\left(\rho_0 \frac{p_d^*(z)}{p_0}\right)$$

$$- \frac{2\alpha}{R^2} J_1 p_d^*(z)$$

$$= -\frac{2\rho_0}{R}[\tilde{u}\bar{\delta} + \widetilde{u''\delta''}] - \frac{\partial}{\partial z}[\rho_0(\overline{w}\bar{\delta} + \overline{w'\delta'})]$$

$$- \rho_0 \frac{\bar{\delta}^2}{2} - \frac{2}{R}\frac{\partial}{\partial z}[\rho_0(\tilde{u}\tilde{w} + \widetilde{u''w''})]. \quad (16)$$

Equations (15) and (16) are the diagnostic equations of buoyancy pressure perturbation and dynamic pressure perturbation, respectively. Combining equations (10) and (13) obtains

$$\bar{\delta} = \frac{2}{R}\tilde{u}. \quad (17)$$

In this model, $\bar{\delta}$ is diagnosed from equation (17) instead of being predicted from equation (8).

We further apply the eddy exchange hypothesis following the notations of Ogura and Takahashi (1971) and Holton (1973). For any variable A, the parameterization formulae are:

$$\widetilde{u''A''} = \frac{v}{R}(\bar{A} - A_0),$$

$$\overline{w'A'} = -K_m \frac{\partial(\bar{A})}{\partial z},$$

where A represents momentum fields. However, if A is a mass field, then K_m is replaced by K_h. v, K_m and K_h are the kinematic viscosity of air, momentum eddy coefficient, and heat eddy coefficient, respectively. The formulae of K_m, K_h, and v are similar to those used in Ogura and Takahashi (1971), and are written as:

$$K_h = v = 3K_m = 0.1 \times R \times |w|.$$

Following the entrainment/detrainment concept in Asai and Kasahara (1967), we assume that the properties of the environment will be brought into clouds (entrainment) if convergence occurs. In contrast, the properties of the clouds will be carried out to the environment (detrainment) if divergence happens, and these detrained properties will be saved and feed back to the resolving grids (e.g. mesoscale model) in the future.

2.2 Cloud microphysical processes

This model includes six classes of hydrometeors: water vapor, cloud water, cloud ice, rain, snow, and graupel. All parameterized microphysical production terms, the last terms on the right-hand side of equations (11) and (12), are based on Lin et al. (1983) and Rutledge and Hobbs (1984). Interactions among these six water substances, such as evaporation/sublimation, deposition/condensation, aggregation, accretion, Bergeron processes, freezing, melting, and melting evaporation, are counted. The formula of each process is given in Appendix B. The saturation adjustment in Tao et al. (1989) is applied. If a layer is supersaturated and cloud water or cloud ice exists, the amount of water vapor condensed to cloud water or deposited to cloud ice depends upon the ratio of cloud ice and cloud water. The same principle is applied to the undersaturated condition. If supersaturation occurs in a layer without cloud ice and cloud water, the ratio of water vapor to cloud water and cloud ice is simply a function of temperature. Furthermore, no water exists when the temperature is less than $-40°C$; liquid and solid phases can coexist when the temperature is between $0°C$ and $-40°C$; graupel or snow can exist without ice crystals when the temperature is above $0°C$.

2.3 Numerical methods

As shown in Fig. 1, a staggered grid is applied. The vertical velocity (w), momentum eddy coefficient (K_m), heat eddy coefficient (K_h), and kinematic viscosity (v) are computed on the full levels. The pressure perturbation (p^*), average lateral radial velocity ($\tilde{u}$), mixing ratios, and temperature fields are calculated on the half levels.

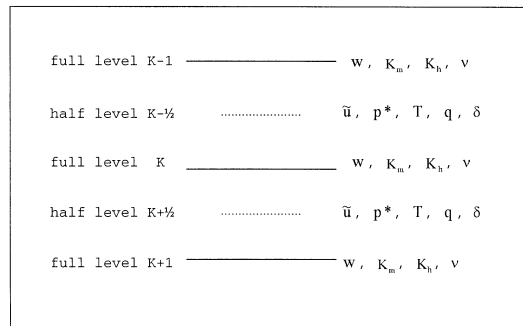The lateral eddy exchange, entrainment, vertical flux, and pressure perturbation gradient

Fig. 1. The model's vertical staggered grid showing full levels and half levels.

force are solved using the Forward-Backward scheme in time (Sun 1984) and using the central difference scheme in space. Vertical fluxes of rain, snow, and graupel due to downward terminal velocities are calculated with a forward scheme. However, to prevent instability from large terminal velocities, a smaller time increment could be used in this part if necessary. A tridiagonal matrix scheme is applied to solve vertical eddy diffusion (implicit scheme), buoyancy pressure perturbation, and dynamic pressure perturbation.

The vertical velocity is zero at both the upper and lower boundaries. The pressure perturbation is zero at the upper boundary, and the normal pressure perturbation gradient is zero at the lower boundary.

3. Comparison with one-dimensional cloud model

The importance of the non-hydrostatic pressure perturbation has been discussed in many papers (List and Lozowski 1970; Holton 1973; Schlesinger 1978; Yau 1979; Kuo and Raymond 1980). Ogura and Takahashi (1971) (hereafter referred to as OT) emphasized that the role of microphysical processes in cloud dynamics is as important as the thermodynamics in clouds. Therefore, the simulation in Section 3 is designed for testing the importance of pressure perturbation and cloud microphysics.

3.1 Initial condition

The initial, boundary, and environmental conditions of this case are from OT, we therefore name this comparison case the OT case. The cloud radius is 3000 m and the surface pressure is 1000 mb. The relative humidity is 100 percent at the lowest level and then decreases with height with a rate of 5% km^{-1}. The temperature is 25°C at the lower boundary. The lapse rate is 6.3°C km^{-1} from the surface to 10 km and then isothermal up to 15 km. A cloud is initiated by weak upward motion in the environment from the surface to 2 km with the formula:

$$w = \left(\frac{z}{z_o}\right)\left(2 - \frac{z}{z_o}\right),$$

where $z_o = 1$ km. The domain is 15 km with a vertical resolution of 200 m. A 5-second time step is used and the model integrates for one

Table 1. Experimental design and results for OT case. The results of OT1 and OT2 can be found in Figures 2a and 3a in OT paper. "Life S." is the life span of a cloud.

Simulation 2	Micro.	P_{nh}	W_{max} ($m\ s_{-1}$)	Life S. (min)
Run 1			20.2	∞
Run 2		x	19.7	∞
Run 3	x		21.6	45
Run 4	x	x	20.4	47
OT1			24-28	∞
OT2		x	16-18	58

hour. Four runs as indicated in Table 1 are tested.

3.2 Results comparison

Table 1 shows that clouds reach a steady state without cloud microphysics (Run 1 and 2) because of the lack of drag forces; therefore, their life spans are infinite. The life span of a cloud is measured from the starting point of the vertical velocity reaching 2 m s^{-1} to the end point of the downward motion (or upward motion) reaching 2 m s^{-1}. When cloud microphysics is included, a cloud grows and eventually dissipates as shown in Fig. 2 and Table 1. The presence of the cloud microphysics produces a positive feedback with respect to the strength of the maximum vertical velocity, either with or without nonhydrostatic pressure (Table 1). However, in OT, the maximum vertical velocity without cloud microphysics, 24–28 m s^{-1} (OT1 in Table 1), is much larger than that with cloud microphysics, 16–18 m s^{-1} (OT2 in Table 1). Besides the different numerical methods used in these two models, the differences between these two models' results could be from the simplification of the cloud microphysics in OT's model. The maximum value of rain mixing ratio reaches 0.01 kg kg^{-1} in our model, but it was only 0.002–
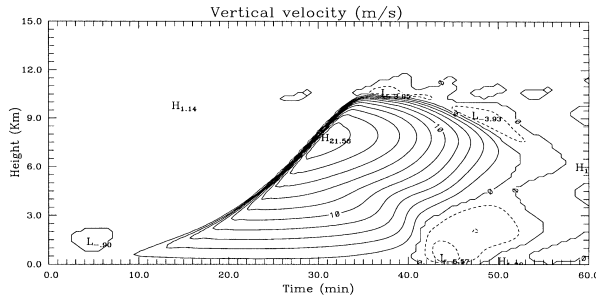
Fig. 2. Time evolution of the vertical velocity with a contour interval of 2 m s^{-1} from the OT case Run 3.

Fig. 3. Time evolution of (a) the vertical velocity with a contour interval of 2 m s^{-1} and (b) the pressure gradient force with a contour interval of 0.03 m s^{-2} from the OT case Run 4.

Fig. 4. Accumulated rain (mm) without nonhydrostatic pressure in Run 3 (line R3) and with nonhydrostatic pressure in Run 4 (line R4) from the OT case.

0.003 kg kg^{-1} in OT (Fig. 3e in OT). The maximum value of the graupel mixing ratio reaches 0.006–0.007 kg kg^{-1} in our model; however graupel, as well as snow, was ignored in OT. Several important processes which might be involved with latent heat were not included in OT, such as the accretion of rain by graupel, rain accretion by cloud ice, accretion of rain by snow, graupel melting to form rain, and accretion of cloud water by rain. In particular, the maximum rate of the accretion of rain by graupel ($\sim 7 \times 10^{-4}$ s^{-1}) is one order larger than the others. At the end of the cloud life cycle, a downward motion develops close to the surface (Fig. 2) due to the drag forces of the precipitation, as well as low level evaporative cooling of rain and the cooling of melting graupel. The precipitation reaches the ground mainly in the form of rain.

Nonhydrostatic pressure perturbation not only reduces the maximum vertical velocity (Table 1), but also weakens the low level downward motion (-2.4 m s^{-1} in Fig. 3a vs. -5.6 m s^{-1} in Fig. 2) because the pressure perturbation gradient force (Fig. 3b) is opposite to the air parcel motion (positive value near the surface during 32 to 40 minutes and negative value at the maximum updraft area). The upward pressure gradient force near the surface also elevates the location of the maximum downward motion. Around cloud top, the upward pressure gradient force helps the cloud reach its mature stage sooner and also helps maintain a longer mature stage (Fig. 2 vs. Fig. 3a). The longer mature stage allows more vigorous microphysical processes (more rain, snow, and graupel are formed), so that the cloud can
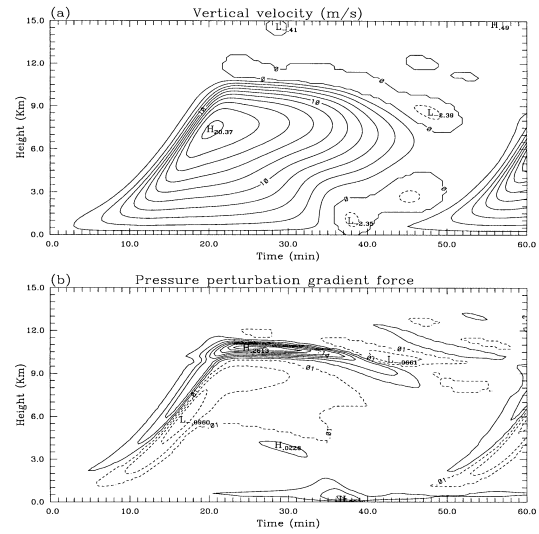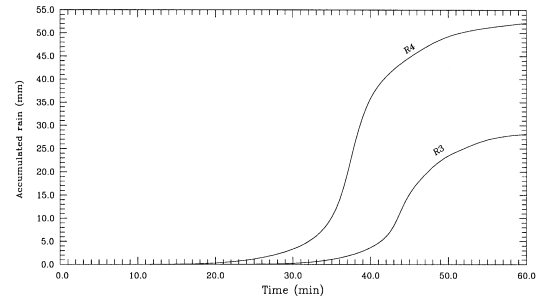
generate more precipitation capable of reaching the ground.

Figure 4 shows the accumulated precipitation amount in both Run 3 and Run 4. The rain falls slowly at the beginning due to the small amount of precipitation, and the upward motion is approximately offset by the terminal velocity. The quasi-suspended situation lets the rain and graupel grow quickly and results in more precipitation, which produces a stronger drag force with time. Besides a stronger drag force, the evaporative cooling of rain and the
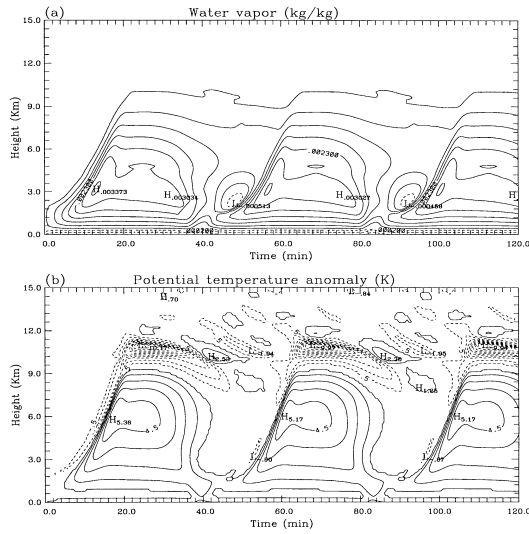
Fig. 5. Time evolution of (a) the water vapor perturbation contoured every 0.0005 kg kg^{-1} and (b) the potential temperature perturbation contoured every 1.0 K from the OT case Run 4.

Fig. 6. Time evolution of (a) water vapor perturbation (contour interval of 0.0005 kg kg^{-1}) and (b) potential temperature perturbation (contour interval of 1.0 K) from the OT case Run 3.

melting of graupel help change the updraft to a downdraft. The downward motion occurs when the precipitation rate reaches its maximum. The rain starts falling earlier in Run 4 and within an hour, 52 mm of precipitation had fallen, while only 28 mm fell in the run without the nonhydrostatic pressure effect. The different qualitative precipitation amount due to the pressure perturbation was also briefly mentioned in Kuo and Raymond (1980).

It is worth mentioning that, in Run 4 (Fig. 3a), as soon as the old cloud dies, a new cell starts growing. Recurrence is also found when nonhydrostatic pressure is excluded, but it takes a much longer time. The recurrence is due to the assumption of the undisturbed surrounding atmosphere during convective development. After the cloud dies, if any disturbance or thermal bubble exists, a new cell may grow. In Run 4, except near the surface, the old cell column is moister (around 40 minutes in Fig. 5a) than the environment after the cell dies. The positive buoyancy (Fig. 5b) and the upward nonhydrostatic pressure gradient force (Fig. 3b) trigger a new upward motion at low levels. However, in Run 3, although the column is slightly warmer than the environment at 40–50 minutes (Fig. 6b) at low levels, a deeper and
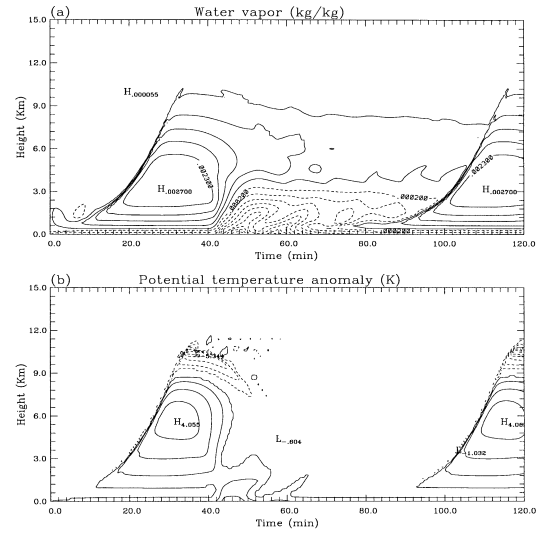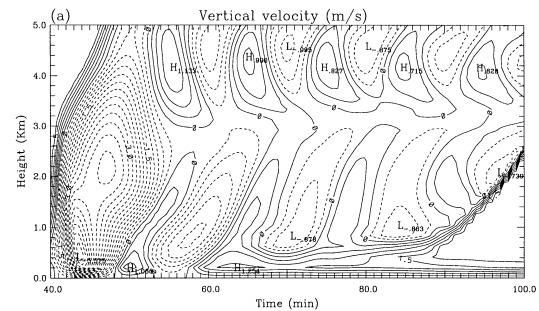

Fig. 7. Time evolution of the vertical velocity with a contour interval of 0.3 m s^{-1} during 40 to 100 minutes below 5 km. For clarity, values greater than 1 m s^{-1} are not contoured.

drier layer in the lower troposphere due to a stronger downward motion (dry advection) prevents a new cell from developing. The moisture perturbation field in Fig. 6a clearly shows that four oscillations occur after the cloud dies, but before the new cell grows. A closer look at these oscillations (Fig. 7) shows that the weak vertical motion creates an opportunity for mixing of the dry, old cell column and the moist environment. The dry layer becomes weaker and weaker and eventually the new cell is able to penetrate it and the cloud starts growing.
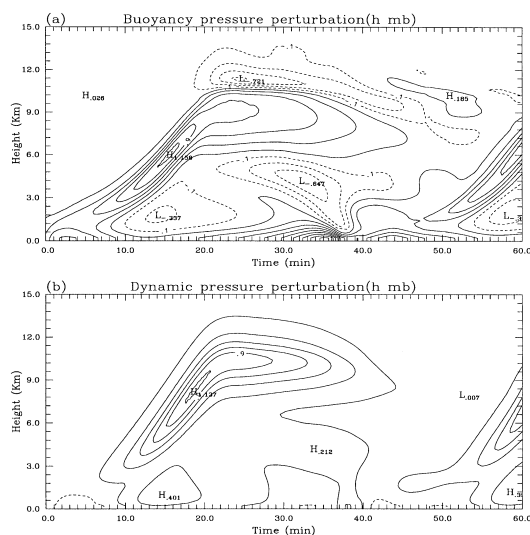
Fig. 8. Time evolution of (a) the buoyancy pressure perturbation and (b) the dynamic pressure perturbation with a contour interval of 0.2 mb from the OT case Run 4.

Figures 5b and 6b show a cold anomaly above the cloud top due to overshooting cooling, but this was not found by OT. We also see that the overshooting cooling of -10.1 K with nonhydrostatic pressure is stronger than that of -5.3 K without nonhydrostatic pressure. The vertical velocity in Run 3 is slightly stronger than that in Run 4 and the cloud top can reach the same height in both runs, but the longer mature stage in Run 4 results in a stronger overshooting cooling. As a result, the presence of the nonhydrostatic pressure perturbation not only decreases the extreme vertical velocities but also increases the precipitation rate, as well as enhances the overshooting cooling above the cloud top.

Figures 8a and 8b show that the meso-high at the cloud top has both buoyancy and dynamic components. Above the cloud top, the negative buoyancy pressure perturbation is opposite to the positive dynamic pressure perturbation. The surface high pressure and the low pressure near 3 km between 25 and 40 minutes, are due to the buoyancy pressure perturbation. The patterns show that the dynamic pressure perturbation is as important as the buoyancy pressure perturbation in this case.

4. A comparison with a three-dimensional cloud model

4.1 Three-dimensional model

The Weather Research and Forecast (WRF) model is a newly-developed, next-generation, fully compressible, nonhydrostatic model which can be applied to both idealized and real weather studies (Michalakes et al. 2001; Skamarock et al. 2001). In this version of the WRF, the governing equations are written in flux form for the purpose of conservation of mass, dry entropy, and scalars. The time split explicit scheme (Klemp and Wilhelmson 1978), the staggered Arakawa C grid, a sigma-height coordinate, a free-slip lower boundary condition, and a rigid upper boundary condition are the features of this model. Several lateral boundary conditions, high order time and space schemes, and physics schemes (Chen and Dudhia 2000) have been implemented. Detailed information for this model can be found on the WRF web site (www.wrf-model.org).

Since the WRF model is used for purposes of comparison, we have chosen from the available schemes ones which most closely match those used in the one-dimensional model, such as the second order Runge-Kutta time scheme (Wicker and Skamarock 1998), the second (third) order advection scheme in the vertical (horizontal), the Smagorinsky's subgrid turbulence scheme (1963). The cloud microphysics scheme is the same as the one in the one-dimensional model. The horizontal resolution, the vertical resolution, and the time step are 1 km, 400 m, and 5 seconds, respectively. The domain size is 92 km $\times$ 92 km $\times$ 20 km in x-y-z direction with open lateral boundary conditions and a 3-km sponge zone at the model top.

4.2 Initial condition

Initial conditions from Schlesinger (1978) (without ambient wind) are used in this experiment. These conditions are typical of the southern Great Plains severe thunderstorm environment. The tropopause is located at 11.9 km, and the atmosphere above this level is assumed to be isothermal up to the upper boundary. The cloud is initiated by a moist thermal bubble as was the trigger function used in Schlesinger (1978), without the vertical velocity perturbation. The formula of the imposed thermal bubble (from the surface to the
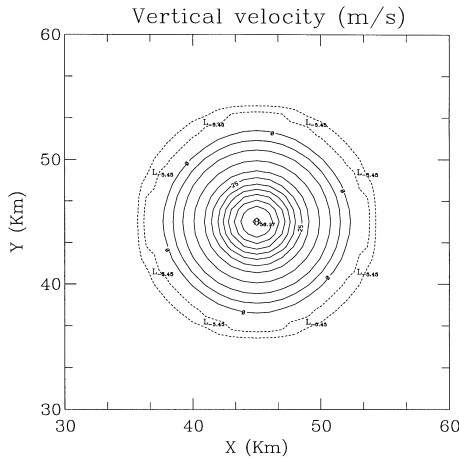
Fig. 9. The horizontal cross section of the vertical velocity (m s^{-1}) of the WRF model at 10 km height after 30-minute integration.

3.5 km) in the WRF is:

$$\theta' = 1.0 \times \sin\left(\frac{\pi \cdot z}{3500}\right) \cdot \exp(-r^2/R^2)$$
$$\cdot (1 - r^2/R^2),$$

where R (= 9 km) is the radius of the bubble, and r is the distance of any grid point to the central vertical axis of the bubble. The thermal perturbation used in the one-dimensional model is from the horizontally averaged value of the three-dimensional bubble. The relative humidity within the cloud (0 to 4.2 km) is 88% for both models, slightly higher than the environment. The same vertical resolution and time resolution are used in the one-dimensional model, but with a smaller vertical domain (16 km).

4.3　Results comparison

Without ambient wind shear, the three-dimensional model produces a cylindrical axisymmetric cloud and the updraft is surrounded by a weak downdraft as shown in Fig. 9. When the updraft reaches its maximum vertical velocity, the maximum radius of the updraft is about 5 km, which is used as the cloud radius in the one-dimensional cloud model. The horizontal averages of the vertical velocity, potential temperature anomaly, and water vapor anomaly within the 5-km radius of updraft from the three-dimensional model are calculated and compared with those from the one-dimensional model.

Figure 10a shows the time evolution of the vertical velocity from the one-dimensional model. The maximum value, 23.7 m s^{-1}, occurs at 9 km after a 17 minute simulation. Figure 10b shows the horizontal-averaged vertical velocity within the radius of 5000 m cloud from the three-dimensional model. There exists two peaks of local maximum values in the three-dimensional model. The larger one is 28.1 m s^{-1} and happens at the 24 minute mark at 11–12 km. The cloud simulated from the one-dimensional model develops earlier, with a slightly weaker intensity for both upward and downward motion. The cloud top is also slightly lower.

The maximum potential temperature anomaly is 7.2 K at 6–7 km around 14 minutes in the one-dimensional model (Fig. 10c) and 7.3 K at 10 km around 23 minutes in the three-dimensional model (Fig. 10d). Both models consistently show that the altitude of the maximum vertical velocity is higher than that of the maximum heating, and the maximum vertical velocity occurs earlier than the maximum heating. Furthermore, both models produce overshooting cooling above the top of the updrafts and cold pool near the surface in the dissipation stage. The overshooting cooling is stronger in the three-dimensional cloud model (−29.8 K vs. −15.3 K), due to a stronger vertical velocity and the penetration into the stratosphere (large potential temperature gradient). The cold pool near the surface in the three-dimensional model is also stronger.

The maximum mixing ratio anomaly of the water vapor in the one-dimensional model is 6.5 g kg^{-1} and happens at 11 minutes at 4.0 km (Fig. 10e), while the maximum is about 6.0 g kg^{-1} at 30 minutes at the same height in the three-dimensional model (Fig. 10f). At the end of the cloud life, the evaporation occurs at lower levels, but it is not enough to compensate the vertical dry advection. Therefore, a drying process exists near the surface in both models. The pressure field (not shown here) indicates that there are two meso-highs in both model results: one is near the cloud top and the other is close to the surface during the downward motion period. However, there is a low near the surface during the developing and mature
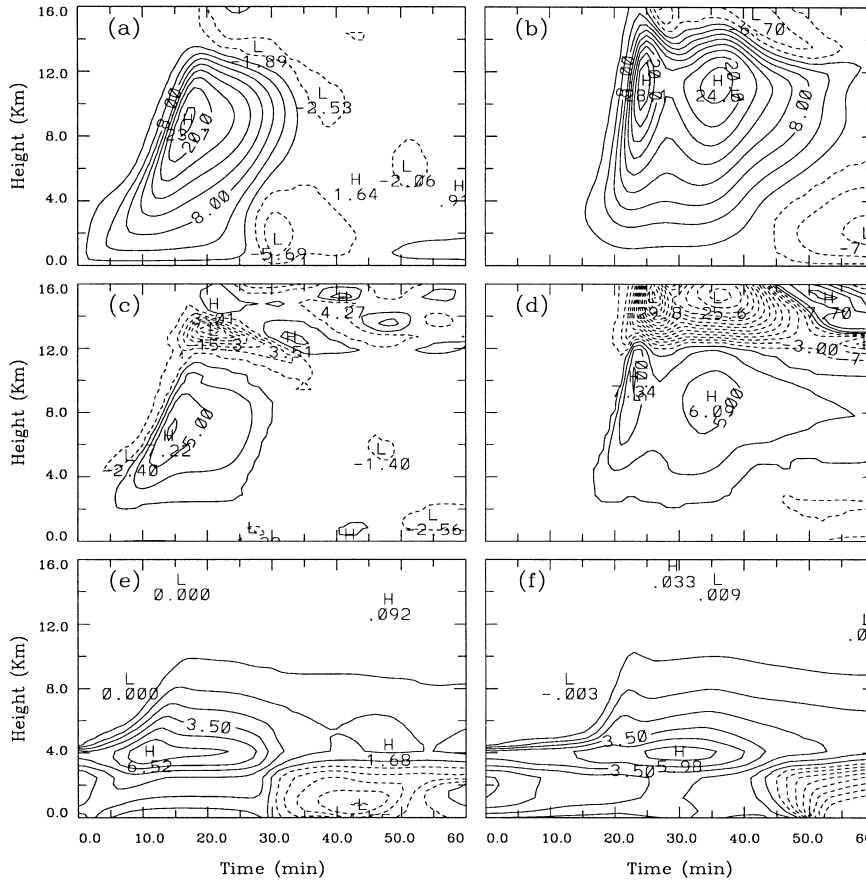
Fig. 10.   Time evolutions of the (a) vertical velocity (m s^{-1}), (c) potential temperature anomaly (K), and (e) moisture anomaly (kg kg^{-1}) from the one-dimensional cloud model, and the averaged (b) vertical velocity (m s^{-1}), (d) potential temperature anomaly (K), and (f) moisture anomaly (kg kg^{-1}) within the radius of 5000 m cloud from the WRF model. The values in (e) and (f) are multiplied by 1×10^3.

stages in the three-dimensional model, but a high in the one-dimensional model.

Besides momentum, thermal, and moisture fields, we also calculate the vertical mass flux (F_m), heat flux (F_h), and moisture flux (F_q) according to the following formulae:

$$F_m = \rho w B,$$

$$F_h = C_p \rho w B (\theta - \theta_0),$$

$$F_q = \rho w B (q_v - q_{v0}),$$

where B is the horizontal area.

In the mass flux field, the maximum values of 9.8×10^8 kg s^{-1} from the one-dimensional model (Fig. 11a) and 9.0×10^8 kg s^{-1} from the three-dimensional model (Fig. 11b) are very close. The patterns of these two models' results

are also comparable, except there are two local maximums and the mass profile is shifted later in time in the three-dimensional simulation.

The maximum vertical heat flux 7.0×10^{12} J s^{-1} in the one-dimensional model (Fig. 11c) is larger than the value 5.7×10^{12} J s^{-1} in the three-dimensional model (Fig. 11d). This is because the density decreases with height. Above the cloud top, the downward heat flux in the one-dimensional model is much smaller than that in the three-dimensional model due to weaker upward motion and weaker overshooting cooling. However, the patterns are still comparable.

The maximum vertical moisture flux in the one-dimensional model (5.2×10^6 kg s^{-1} in Fig. 11e) is larger than that in the three-dimen-
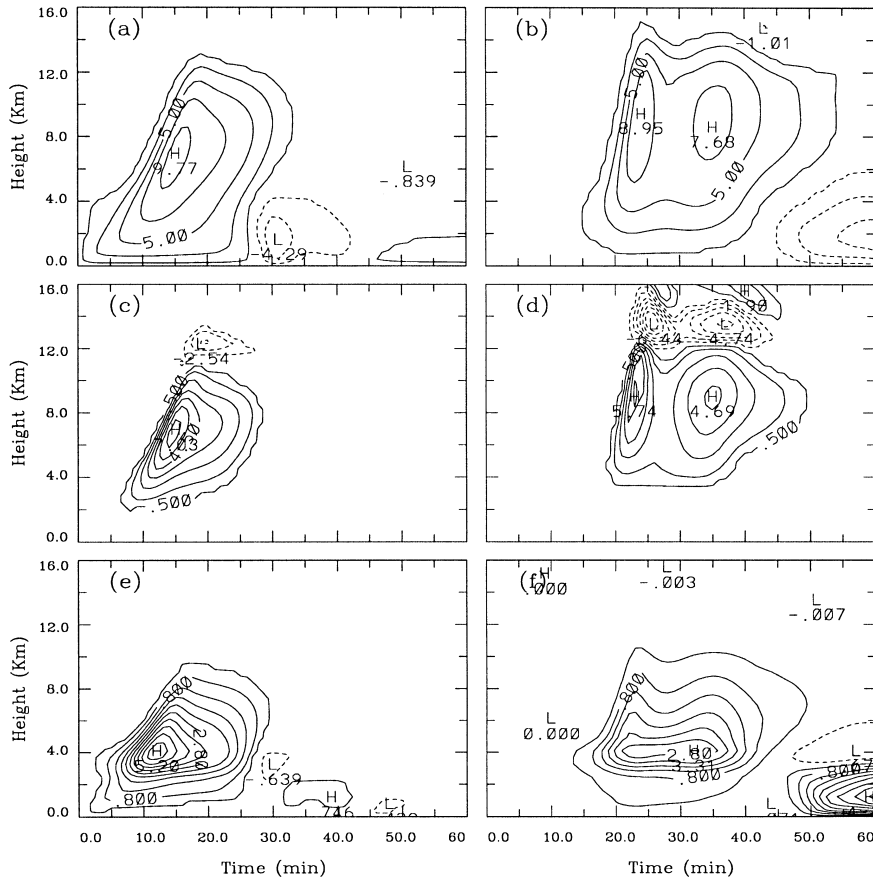
Fig. 11. Time evolutions of the (a) mass flux ($\times 10^8$ kg s^{-1}), (c) heat flux ($\times 10^{12}$ J s^{-1}), and (e) moisture flux ($\times 10^6$ kg s^{-1}) from the one-dimensional cloud model, and the averaged (b) mass flux ($\times 10^8$ kg s^{-1}), (d) heat flux ($\times 10^{12}$ J s^{-1}), and (f) moisture flux ($\times 10^6$ kg s^{-1}) within the radius of 5000 m cloud from the WRF model.

sional model (3.3×10^6 kg s^{-1} in Fig. 11f). The heights of the maximum values and the patterns are quite similar. The positive anomaly, which occurs near the surface during the dissipation stage, is much stronger in the three-dimensional model due to stronger downward motion and a stronger drying process.

Figure 12 shows the accumulated precipitation from both model simulations. The three-dimensional result still uses the horizontally averaged value within the 5000 m cloud radius. The precipitation in the one-dimensional model occurs earlier and is concentrated between 20 and 35 minutes, while the precipitation in the three-dimensional model occurs later and at a more gradual rate. After 90 minutes, the accu-
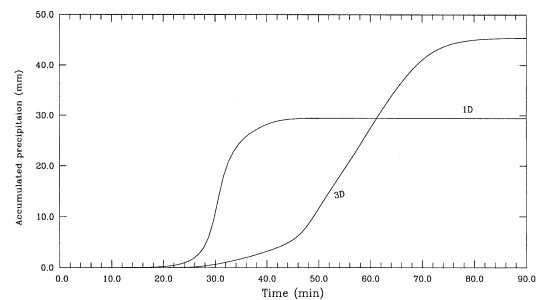

Fig. 12. Accumulated rain (mm) (a) from the one-dimensional cloud model, and (b) from the WRF model (averaged within the radius of 5000 m).
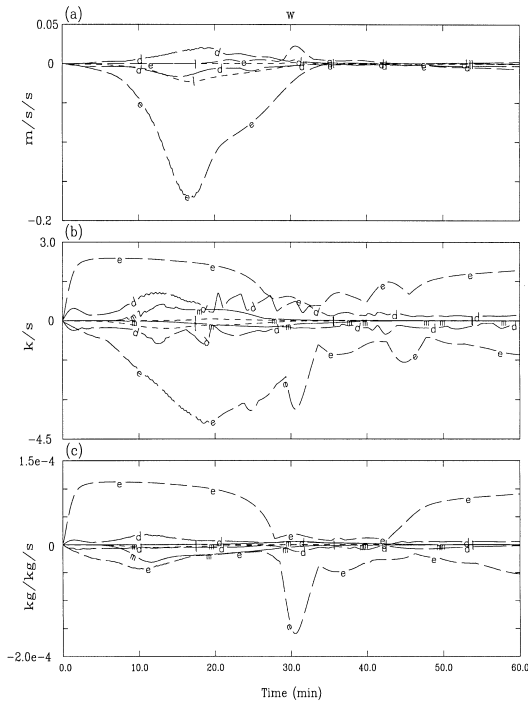
Fig. 13. Time evolution of the maximum and minimum rates of several forcing terms, such as entrainment (—e—) (positive), lateral eddy diffusion (—l—), vertical diffusion (—d—), and cloud microphysics (—m—), from the one-dimensional cloud model for (a) vertical momentum equation (m s^{-2}), (b) thermodynamic equation (K s^{-1}), and (c) non-precipitable water equation (kg kg^{-1} s^{-1}). In (b), the lateral eddy diffusion, vertical diffusion, and cloud microphysics are multiplied by 20 for visualization.

mulated precipitation amount reaches 46 mm for the three-dimensional model, while it is only 29 mm for the one-dimensional model.

4.4 Entrainment, lateral eddy diffusion, vertical diffusion, and microphysics in the one-dimensional cloud model

The forcing terms of the entrainment, lateral eddy diffusion, vertical diffusion, and cloud microphysics in the one-dimensional cloud model are calculated. Figure 13 shows the time evolution of the maximum and minimum values of each term for the vertical momentum, thermo-

dynamic, and non-precipitable water equations. The results indicate that the entrainment effect is very important for all prognostic variables (the same conclusion for others). During the updraft period, the entrainment (detrainment) occurs at lower (upper) levels (Fig. 14a). The vertical momentum detrains out from the upper portion of the cloud (negative value in Fig. 13a), while no momentum entrains into the cloud at lower levels since the surroundings are calm in this case. The positive entrainment rate in the first 28 minutes matches quite well for both equivalent ice potential temperature and non-precipitable water (q_w) since the environment entrains high θ_{ei} and q_w into the cloud (Fig. 14a). The detrainment rate of q_w at upper levels is relatively smaller than the entrainment rate at lower levels (Fig. 13c and Fig. 14a) since a lot of q_w has been transformed into rain, snow, and graupel when the moist air ascends. Figure 13 also shows another peak of detrainment rate in association with the downward motion (30 minutes). It is noted that the high entrainment rate is mostly concentrated at the lowest two to three levels, while the detainment rate is gradually spread out at the upper portion of the cloud. The detrainment could extend to 5-km depth (more than one layer) for the equivalent ice potential temperature (figure is not shown here). This entrainment/detrainment process is very important for the vertical exchange of surrounding air and for the cloud information contributed from the subgrid scale.

For the q_w, the microphysics is a sink term inside the updraft (Fig. 14b), but it becomes a source term during the downward motion (evaporation from rain). The maximum transformation rate from q_w to rain, snow, and graupel (microphysical processes) is comparable to that detrained out from upper levels of the updraft. For the equivalent ice potential temperature, the microphysics is a source (sink) term above (below) the melting level. It is worth mentioning that the rate of change of the equivalent ice potential temperature due to cloud microphysics is very small (only 1% of that due to entrainment/detrainment) since the change only occurs when the snow or graupel amount varies in microphysical processes. The vertical diffusion (Fig. 14c) is a downgradient process, namely reducing the difference be-

Fig. 14. Time evolution of the rate of change of non-precipitable water (kg kg^{-1} s^{-1}) due to (a) entrainment, (b) microphysics, (c) vertical eddy diffusion, and (d) lateral eddy. The values are multiplied by 1×10^6 for visualization. The contour interval is 20 kg kg^{-1} s^{-1} for entrainment and 2 kg kg^{-1} s^{-1} for the others.

tween the maximums and minimums, and the lateral diffusion (Fig. 14d) is a sink term for the cloud during the updraft period.

5. Summary

A one-dimensional cloud model is developed for possible use in the cumulus parameterization scheme developed by Sun and Haines (1996). The effects of entrainment, cloud microphysics, pressure perturbation, lateral eddy diffusion, and vertical eddy diffusion are taken into account. The inclusion of nonhydrostatic pressure could (1) reduce the vertical velocities, (2) help the cloud develop sooner, (3) help maintain a longer mature stage, (4) produce a stronger overshoot cooling, and (5) approximately double the precipitation amount. Simu-

lations also indicate that both the dynamic pressure perturbation and the buoyancy pressure perturbation are equally important to the formation of a cloud. The analysis of the forcing terms for entrainment, cloud microphysics, lateral eddy diffusion, and vertical eddy diffusion shows that the entrainment effect dominates the other three for a cloud development. In addition, the detrainment layer could extend over a 5-km depth (more than one layer) for equivalent ice potential temperature.

Two comparisons are examined in this study: a one-dimensional cloud model (Ogura and Takahashi 1971) and a three-dimensional Weather Research and Forecast (WRF) model (Michalakes et al. 2001; Skamarock et al. 2001). Our simulation shows that the inclusion of cloud

microphysics develops a stronger cloud. However, this is quite different from those presented in Ogura and Takahashi (1971), which had simplified cloud microphysics. In our simulations, several microphysical processes related to graupel are quite important (e.g., the accretion of rain by graupel, rain accretion by cloud ice, accretion of rain by snow, graupel melting to form rain, and accretion of cloud water by rain), but these were not counted in Ogura and Takahashi (1971).

No ambient wind shear is considered in the comparison with a three-dimensional cloud model. The horizontally averaged results within the three-dimensional cloud were used to do the comparison. The one-dimensional model is capable of reproducing the major features of a convective cloud generated by the three-dimensional model, such as fluxes, cold pool, overshooting cooling, and two meso-highs. Some differences (e.g., double maximum peaks and the meso-low) existing between both model results should not be surprising because clouds simulated from a three-dimensional model are quite nonlinear. Hence, those features may be difficult to be reproduced by a one-dimensional model. It is also noted that the environment remains as the initial condition in the one-dimensional model, but it changes with time in three-dimensional simulations. Definitely, there is room for improvement of this one-dimensional cloud model.

The tilting of convective clouds has often been observed and it might influence a cloud's life, properties, and rain rate. The importance of the downdraft, which develops besides the updraft, has also received lots of attention. The tilting of the cloud might be related to the surrounding wind shear, and it will be an interesting subject to study their relationship. Besides applying this model to a cumulus parameterization scheme, we will keep improving this one-dimensional model, especially the consideration of the downdraft effect.

Acknowledgments

Appendix A

The horizontal average of the vertical momentum equation

Since the derivations of all equations are very similar, we only present the vertical momentum equation here. The horizontal average of equation (1) is derived term by term as follows:

$$\frac{1}{\pi R^2}\int_0^{2\pi}\int_0^R \frac{\partial w}{\partial t} r\,dr\,d\psi = \frac{\partial \overline{w}}{\partial t}.$$

$$-\frac{1}{\pi R^2}\int_0^{2\pi}\int_0^R \frac{1}{r}\frac{\partial(urw)}{\partial r} r\,dr\,d\psi$$

$$= -\frac{1}{\pi R^2}\int_0^{2\pi}[(urw)]\big|_0^R\,d\psi$$

$$= -\frac{1}{\pi R}\int_0^{2\pi}(uw)\,d\psi$$

$$= -\frac{2}{R}\widetilde{uw}$$

$$= -\frac{2}{R}(\tilde{u}\tilde{w} + \widetilde{u''w''}).$$

Here, we assume that $\tilde{u}(\tilde{w})$ and $w''(u'')$ are uncorrelated.

$$-\frac{1}{\pi R^2}\int_0^{2\pi}\int_0^R \frac{1}{r}\frac{\partial(vw)}{\partial \psi} r\,dr\,d\psi$$

$$= -\frac{1}{\pi R^2}\int_0^R \left[\frac{\partial(vw)}{\partial \psi}\right]\bigg|_0^{2\pi}\,dr$$

$$= 0.$$

$$-\frac{1}{\pi R^2}\int_0^{2\pi}\int_0^R \frac{1}{\rho_0}\frac{\partial(\rho_0 w^2)}{\partial z} r\,dr\,d\psi$$

$$= -\frac{1}{\rho_0}\frac{\partial}{\partial z}\left[\rho_0\frac{1}{\pi R^2}\int_0^{2\pi}\int_0^R w^2 r\,dr\,d\psi\right]$$

$$= -\frac{1}{\rho_0}\frac{\partial}{\partial z}(\rho_0\overline{ww})$$

$$= -\frac{1}{\rho_0}\frac{\partial}{\partial z}[\rho_0(\overline{w}\,\overline{w} + \overline{w'w'})].$$

$\overline{w}$ and w' are also assumed uncorrelated. ρ_0 is only function of height.

$$-\frac{1}{\pi R^2}\int_0^{2\pi}\int_0^R \frac{1}{\rho_0}\frac{\partial p_{nh}}{\partial z}r\,dr\,d\psi$$

$$=-\frac{1}{\rho_0}\frac{\partial p^*}{\partial z}\frac{1}{\pi R^2}\int_0^{2\pi}\int_0^R J_0(r)r\,dr\,d\psi$$

$$=-\frac{1}{\rho_0}\frac{\partial p^*}{\partial z}\frac{1}{\pi R^2}\cdot 2\pi\cdot\frac{R^2}{\alpha^2}\int_0^\alpha J_0(x)x\,dx$$

$$=-\frac{2}{\rho_0}\frac{\partial p^*}{\partial z}\frac{1}{\alpha^2}\left[xJ_1(x)\right]|_0^\alpha$$

$$=-\frac{2J_1(\alpha)}{\rho_0\alpha}\frac{\partial p^*}{\partial z},$$

where $x=\frac{\alpha}{R}\cdot r$ and $p_{nh}(r,z)=p^*(z)\cdot J_0(r)$ as mentioned in Section 2.

$$\frac{1}{\pi R^2}\int_0^{2\pi}\int_0^R g\frac{(\theta_v-\theta_{v0})}{\theta_{v0}}r\,dr\,d\psi=g\frac{(\bar\theta_v-\theta_{v0})}{\theta_{v0}}.$$

$$\frac{1}{\pi R^2}\int_0^{2\pi}\int_0^R g\left(\frac{R}{C_p}-1\right)\frac{p_{nh}}{p_0}r\,dr\,d\psi$$

$$=\frac{g}{p_0}\left(\frac{R}{C_p}-1\right)p^*(z)\frac{1}{\pi R^2}\int_0^{2\pi}\int_0^R J_0(r)r\,dr\,d\psi$$

$$=g\left(\frac{R}{C_p}-1\right)\frac{2J_1(\alpha)}{\alpha}\frac{p^*(z)}{p_0}.$$

$$-\frac{1}{\pi R^2}\int_0^{2\pi}\int_0^R gQ_T r\,dr\,d\psi=-g\bar Q_T.$$

Appendix B

Bulk parameterization of cloud microphysics

The formulae for microphysical processes are based on Lin et al. (1983) and Rutledge and Hobbs (1984). The size distribution of the rain, snow and graupel are hypothesized as:

$$N_r(D_r)=N_{or}\exp(-\lambda_r D_r),$$

$$N_s(D_s)=N_{os}\exp(-\lambda_s D_s),$$

$$N_g(D_g)=N_{og}\exp(-\lambda_g D_g),$$

where N_{or}, N_{os} and N_{og} are the intercept parameters of the rain, snow and graupel size distributions, respectively. D_r, D_s and D_g are diameters of the rain, snow and graupel particles, respectively. The slope parameters of the rain, snow and graupel size distributions (λ_r, λ_s and λ_g) are written as:

$$\lambda_r=\left(\frac{\pi\rho_w N_{or}}{\rho q_r}\right)^{1/4},$$

$$\lambda_s=\left(\frac{\pi\rho_s N_{os}}{\rho q_s}\right)^{1/4},$$

$$\lambda_g=\left(\frac{\pi\rho_g N_{og}}{\rho q_g}\right)^{1/4}.$$

ρ_w, ρ_s, and ρ_g are densities of rain, snow, and graupel, respectively. The terminal velocities of the rain, snow and graupel particles are:

$$U_r(D_r)=aD_r^b\left(\frac{\rho_o}{\rho}\right)^{1/2},$$

$$U_s(D_s)=cD_s^d\left(\frac{\rho_o}{\rho}\right)^{1/2},$$

$$U_g(D_g)=\left(\frac{4g\rho_g}{3C_D\rho}\right)^{1/2}D_g^{1/2}.$$

where $b=0.8$, $a=2115\times0.01^{(1-b)}$, $d=0.25$, $c=152.93\times0.01^{(1-d)}$, $\rho_o=1.29$ kg m^{-3}, and C_D (a drag coefficient) $=0.6$. The mass-weighted mean terminal velocities of the rain, snow and graupel are:

$$U_r=\frac{a\Gamma(4+b)}{6\lambda_r^b}\left(\frac{\rho_o}{\rho}\right)^{1/2},$$

$$U_s=\frac{c\Gamma(4+d)}{6\lambda_s^d}\left(\frac{\rho_o}{\rho}\right)^{1/2},$$

$$U_g=\frac{\Gamma(4.5)}{6\lambda_g^{0.5}}\left(\frac{4g\rho_g}{3C_D\rho}\right)^{1/2}.$$

Γ is the gamma function.

A.1　Aggregation

The aggregation rate of ice crystals to form snow is:

$$\alpha_1=1.0\times10^{-3}\exp(0.025T_c),$$

$$P_{saut}=\alpha_1(q_i-q_{io}),$$

where α_1 is a rate coefficient (s^{-1}), T_c is the temperature in the units of °C, and q_{io} ($=1.E-3$ kg kg^{-1}) is a threshold amount for aggregation to occur.

The collision and coalescence of cloud droplets to form raindrops is:

$$P_{raut}=0.001\times(q_c-q_{co}),$$

where q_{co} ($= 7.E-4$ kg kg^{-1}) is a threshold for autoconversion.

A.2 Accretion

The rate of accretion of cloud ice by snow is:

$$P_{saci} = \frac{\pi E_{SI} N_{os} c q_i \Gamma(3+d)}{4\lambda_s^{3+d}} \left(\frac{\rho_o}{\rho}\right)^{1/2},$$

where E_{SI}, the collection efficiency of the snow for cloud ice, is a function of temperature and expressed as:

$$E_{SI} = \exp(0.025T_c).$$

The accretion rate of cloud water by snow is:

$$P_{sacw} = \frac{\pi E_{SW} N_{os} c q_c \Gamma(3+d)}{4\lambda_s^{3+d}} \left(\frac{\rho_o}{\rho}\right)^{1/2},$$

where E_{SW}, the collection efficiency of the snow for cloud water, is assumed to be 1. When $T_c < 0^\circ$C, P_{sacw} will increase the snow content. Otherwise, it will contribute to rain content.

The accretion rate of cloud ice by rain is:

$$P_{raci} = \frac{\pi E_{RI} N_{or} a q_i \Gamma(3+b)}{4\lambda_r^{3+b}} \left(\frac{\rho_o}{\rho}\right)^{1/2},$$

where E_{RI}, the collection efficiency of the rain for cloud ice, is assumed to be 1.

$$P_{iacr} = \frac{\rho \pi^2 E_{RI} N_{or} a q_i \rho_w \Gamma(6+b)}{24 M_i \lambda_r^{6+b}} \left(\frac{\rho_o}{\rho}\right)^{1/2},$$

where $M_i = 4.19 \times 10^{-13}$ kg.

The accretion rate of rain by snow, P_{racs}, and snow by rain, P_{sacr}, are:

$$P_{racs} = \pi^2 E_{SR} N_{or} N_{os} |U_r - U_s| \left(\frac{\rho_s}{\rho}\right)$$
$$\times \left(\frac{5}{\lambda_s^6 \lambda_r} + \frac{2}{\lambda_s^5 \lambda_r^2} + \frac{0.5}{\lambda_s^4 \lambda_r^3}\right),$$

$$P_{sacr} = \pi^2 E_{SR} N_{os} N_{or} |U_r - U_s| \left(\frac{\rho_w}{\rho}\right)$$
$$\times \left(\frac{5}{\lambda_r^6 \lambda_s} + \frac{2}{\lambda_r^5 \lambda_s^2} + \frac{0.5}{\lambda_r^4 \lambda_s^3}\right),$$

where $E_{SR} = 1$.

The accretion rate of snow by graupel, P_{gacs} is:

$$P_{gacs} = \pi^2 E_{GS} N_{os} N_{og} |U_g - U_s| \left(\frac{\rho_s}{\rho}\right)$$
$$\times \left(\frac{5}{\lambda_s^6 \lambda_g} + \frac{2}{\lambda_s^5 \lambda_g^2} + \frac{0.5}{\lambda_s^4 \lambda_g^3}\right),$$

where $E_{GS} = \exp(0.09T_c)$ when $T_c < 0^\circ$, and $E_{GS} = 1.0$ when $T_c >= 0^\circ$.

Hail grows by accretion of other water forms in either the dry (P_{gdry}) or wet (P_{gwet}) growth mode. The mode with smaller amount is chosen.

$$P_{gdry} = P_{gacw} + P_{gaci} + P_{gacr} + P_{gacs}.$$

The rate of graupel accretion cloud water (P_{gacw}), cloud ice (P_{gaci}), and rain (P_{gacr}) are:

$$P_{gacw} = \frac{\pi E_{GW} N_{og} q_c \Gamma(3.5)}{4\lambda_g^{3.5}} \left(\frac{4g\rho_g}{3C_D \rho}\right)^{1/2},$$

$$P_{gaci} = \frac{\pi E_{GI} N_{og} q_i \Gamma(3.5)}{4\lambda_g^{3.5}} \left(\frac{4g\rho_g}{3C_D \rho}\right)^{1/2},$$

$$P_{gacr} = \pi^2 E_{GR} N_{og} N_{or} \frac{\rho_w}{\rho} |U_g - U_r|$$
$$\times \left(\frac{5}{\lambda_r^6 \lambda_g} + \frac{2}{\lambda_r^5 \lambda_g^2} + \frac{0.5}{\lambda_r^4 \lambda_g^3}\right),$$

where $E_{GW} = 1$, $E_{GR} = 1$, and E_{GI} is assumed to be 0.1 and 1 for dry and wet growth, respectively.

$$P_{gwet} = \frac{2\pi N_{og} (\rho L_v \psi \triangle r_s - K_a T_c)}{\rho (L_f + C_w T_c)}$$
$$\times \left[0.78\lambda_g^{-2} + 0.31 S_c^{1/3} \Gamma(2.75)\right.$$
$$\times \left.\left(\frac{4g\rho_g}{3C_D}\right) v^{-1/2} \lambda_g^{-2.75}\right]$$
$$+ (P'_{gaci} + P'_{gacs})\left(1 - \frac{C_i T_c}{L_f + C_w T_c}\right),$$

and

$$P'_{gacr} = P_{gwet} - P_{gacw} - P'_{gaci} - P'_{gacs},$$

where the formula for P'_{gaci} is given as P_{gaci} with $E_{GI} = 1$ and similarly the formula for P'_{gacs} is given as P_{gacs} with $E_{GS} = 1$. ψ, $\triangle r_s$, K_a, C_w, and C_i are the diffusivity of water vapor in air, water vapor mixing ratio difference between saturation and the environment, thermal conductivity of air, and the specific heats of water and ice, respectively.

The accretion rate of cloud water by rain is:

$$P_{racw} = \frac{\pi E_{RW} N_{or} a q_c \Gamma(3+b)}{4\lambda_r^{3+b}} \left(\frac{\rho_o}{\rho}\right)^{1/2}.$$

where $E_{RW} = 1$.

A.3 Bergeron processes

Two terms, P_{sfw} and P_{sfi}, describe the rates at which cloud water and cloud ice, respectively, transform to snow by deposition and riming according to the growth of a 50 µm radius ice crystal.

$$P_{sfw} = N_{I50}(a_1 m_{I50}^{a_2} + \pi E_{IW} \rho q_c R_{I50}^2 U_{I50}),$$

$$P_{sfi} = \frac{q_i}{\triangle t_1},$$

where a_1 and a_2 are temperature dependent parameters in the Bergeron process (Koenig 1971), and N_{I50}, R_{I50} $(= 1.0E-4$ m), m_{I50} $(= 4.8E-10$ kg) and U_{I50} are the number concentration (g^{-1}), the radius, mass and terminal velocity of a 50 µm size ice crystal (Hsie et al. 1980). The collection efficiency of cloud ice for cloud water, E_{IW}, is assumed to be 1. The time needed for a crystal to grow from 40 to 50 µm is given by

$$\triangle t_1 = \frac{1}{a_1(1-a_2)}[m_{I50}^{(1-a_2)} - m_{I40}^{(1-a_2)}],$$

where m_{I40} $(= 2.46E-10$ kg) is the mass of a 40 µm size ice crystal.

A.4 Deposition (or sublimation)

The depositional growth rate of snow, P_{sdep} is:

P_{sdep} (or P_{ssub})

$$= \frac{2\pi(S_i - 1)}{\rho(A'' + B'')} N_{os} \times \left[0.78\lambda_s^{-2} + 0.31 S_c^{1/3}\Gamma \right.$$
$$\left. \times \left(\frac{d+5}{2}\right) c^{1/2} \left(\frac{\rho_o}{\rho}\right)^{1/4} v^{-1/2} \lambda_s^{-(d+5)/2}\right],$$

where

$$A'' = \frac{L_s^2}{K_a R_w T^2},$$

$$B'' = \frac{1}{\rho q_{si} \psi}.$$

R_w, v, S_i, and S_c are specific gas constant for water vapor, kinematic viscosity of air, saturation ratio over ice, and Schmidt number

$(= v/\psi)$, respectively. T is the temperature in the Kelvin units.

The sublimation of hail will occur at the subsaturated region and the formula is:

P_{gdep} (or P_{gsub})

$$= \frac{2\pi(S_i - 1)}{\rho(A'' + B'')} N_{og} \left[0.78\lambda_g^{-2} \right.$$
$$\left. + 0.31 S_c^{1/3}\Gamma(2.75)\frac{4g\rho_g}{3C_D\rho}^{1/4} v^{-1/2}\lambda_g^{-2.75}\right].$$

A.5 Melting and melting evaporation

The melting of snow is:

$$P_{smlt} = -\frac{2\pi}{\rho L_f}(K_a T_c - L_v \psi \rho \triangle r_s)N_{os}$$
$$\times \left[0.78\lambda_s^{-2} + 0.31 S_c^{1/3}\Gamma\left(\frac{d+5}{2}\right)c^{1/2}\right.$$
$$\left. \times \left(\frac{\rho_o}{\rho}\right)^{1/4} v^{-1/2}\lambda_s^{-(d+5)/2}\right]$$
$$-\frac{C_w T_c}{L_f}(P_{sacw} + P_{sacr}).$$

The rate of evaporation of melting snow is

$$P_{smltevp} = \frac{2\pi N_{os}(S-1)}{\rho(C'' + D'')}$$
$$\times \left[\frac{0.78}{\lambda_s^2} + \frac{0.31 S_c^{1/3} c^{1/2}\Gamma\left(\frac{d+5}{2}\right)}{v^{1/2}\lambda_s^{(d+5)/2}}\left(\frac{\rho_o}{\rho}\right)^{1/4}\right].$$

The rate of evaporation of melting graupel is:

$$P_{gmltevp} = \frac{2\pi N_{og}(S-1)}{C'' + D''}\frac{0.78}{\lambda_g^2}$$
$$+ 0.31\left(\frac{\bar{a}\rho}{v}\right)^{1/2}\left(\frac{p_{oo}^{0.2}}{p}\right)\frac{\Gamma(\bar{b}/2 + 5/2)}{\lambda_g^{\bar{b}/2 + 5/2}},$$

where

$$C'' = \frac{L_v}{K_a T}\left(\frac{L_v M_w}{R^* T} - 1\right),$$

$$D'' = \frac{R^* T}{\psi M_w e_{sw}}.$$

$\bar{b}$ $(= 0.37)$ is the fallspeed exponent for graupel; $\bar{a}$ $(= 19.3$ m$^{(1-\bar{b})}$ s$^{-1})$ is a constant in the fallspeed relation for graupel; M_w $(= 18.0160)$ is the molecular weight of water; e_{sw} is a saturation vapor pressure for water; R^* is the universal gas constant.

The melting of graupel is:

$$P_{gmlt} = -\frac{2\pi}{\rho L_f}(K_a T_c - L_v \psi \rho \triangle r_s)N_{og}$$

$$\times \left[0.78\lambda_g^{-2} + 0.31S_c^{1/3}\Gamma(2.75) \right.$$

$$\times \left(\frac{4g\rho_g}{3C_D} \right)^{1/4} \nu^{-1/2}\lambda_g^{-2.75} \right]$$

$$-\frac{C_w T_c}{L_f}(P_{gacw} + P_{gacr}).$$

A.6 Snow crystal aggregation

Rimed snow crystals may collide and aggregate to form graupel. The formula is:

$$P_{gaut} = \alpha_2(q_s - q_{so}),$$

where α_2 ($= 10^{-3}\exp(0.09T_c)$) is a rate coefficient (s^{-1}), and q_{so} ($= 6.E-4$ kg kg^{-1}) is a mass threshold of snow.

A.7 Raindrop freezing

The probabilistic freezing of rain to form graupel is given as:

$$P_{gfr} = 20\pi^2 B'N_{or}\left[\frac{\rho_w}{\rho} \times [\exp(-A'(T_c)) - 1]\right]\lambda_r^{-7},$$

where $A' = 0.66$ K^{-1}, and $B' = 100$ m^{-3} s^{-1}.

A.8 Evaporation

The evaporation rate for rain is:

$$P_{revp} = \frac{2\pi(S-1)N_{or}}{\rho(C'' + D'')}$$

$$\times \left[\frac{0.78}{\lambda_r^2} + \frac{0.31S_c^{1/3}\Gamma\left(\frac{b+5}{2}\right)a^{1/2}}{\nu^{1/2}\lambda_r^{-(b+5)/2}}\left(\frac{\rho_o}{\rho}\right)^{1/4}\right]$$

$$\times \left[\frac{1}{\rho}\left(\frac{L_v^2}{K_a R_w T^2} + \frac{1}{\rho q_{sw}\psi}\right)^{-1}\right].$$

where S is the saturation ratio, and q_{sw} is the saturation mixing ratio of water vapor with respect to water.

References

Arakawa, A. and W. Schubert, 1974: Interaction of a cumulus cloud ensemble with the large-scale environment, Part I. *J. Atmos. Sci.*, **31**, 674–701.

Asai, T. and A. Kasahara, 1967: A theoretical study of the compensating downward motions associated with cumulus clouds. *J. Atmos. Sci.*, **24**, 487–496.

Betts, A.K., 1986: New convective adjustment scheme, Part I, Observational and theoretical basis. *Quart. J. Roy. Meteor. Soc.*, **112**, 677–691.

Chen, S.-H. and J. Dudhia, 2000: Annual report: WRF physics (www.wrf-model.org). 38pp.

Cheng, M.-D., 1989a: Effects of downdrafts and mesoscale convective organization on the heat and moisture budgets of tropical cloud clusters. Part I: A diagnostic cumulus ensemble model. *J. Atmos. Sci.*, **46**, 1517–1538.

Chern, D.C., 1994: Numerical simulations of cyclogenesis over the western United States. Ph. D. Thesis, Purdue University, 178 pp.

Ferrier, B.S. and R.A. Houze, 1989: One-dimensional time-dependent modeling of GATE cumulonimbus convection. *J. Atmos. Sci.*, **46**, 330–352.

Fritsch, J.M. and C.F. Chappell, 1980: Numerical prediction of convectively driven mesoscale pressure system. Part I: Convective parameterization. *J. Atmos. Sci.*, **37**, 1722–1733.

Grell, G.A., 1993: Prognostic evaluation of assumptions used by cumulus parameterizations. *Mon. Wea. Rev.*, **121**, 764–787.

Haines, P.A., 1992: Numerical simulation of a squall line: Tests of a new cumulus parameterization scheme. Ph. D. Thesis, Purdue University, 389 pp.

—— and W.Y. Sun, 1994: A convective cloud model for use in a cumulus parameterization scheme. *Mon. Wea. Rev.*, **122**, 165–182.

Hsie, E.Y., R.D. Farely, and H.D. Orville, 1980: Numerical simulation of ice-phase convective cloud seeding. *J. Appl. Meteor.*, **19**, 950–977.

Holton, J.R., 1973: A one-dimensional cumulus model including presure perturbations. *Mon. Wea. Rev.*, **101**, 201–205.

Kain, J.S. and R.B. Wilhelmson, 1978: Simulation of three-dimensional convective storm dynamics. *J. Atmos. Sci.*, **35**, 1070–1110.

—— and J.M. Fritsch, 1990: A one-dimensional entraining/detraining plume model and its application in convective parameterization. *J. Atmos. Sci.*, **47**, 2784–2802.

Klemp, J.B. and R. Wilhelmson, 1978: The simulation of three-dimensional convective storm dynamics. *J. Atmos. Sci.*, **35**, 1070–1096.

Koenig, L.R., 1971: Numerical modeling of ice deposition. *J. Atmos. Sci.*, **28**, 226–237.

Kuo, H.L., 1974: Further studies of the parameterization of the influence of cumulus convection on large-scale flow. *J. Atmos. Sci.*, **31**, 1232–1240.

—— and W.H. Raymond, 1980: A quasi-one-dimensional cumulus cloud model and parameterization of cumulus heating and mixing effects. *Mon. Wea. Rev.*, **108**, 991–1009.

Levi, L. and M.E. Saluzzi, 1996: Effects of ice formation on convective cloud development. *J. Appl. Meteor.*, **35**, 1587–1595.

Lin, Y.-L., R.D. Farley, and H.D. Orville, 1983: Bulk parameterization of the snow field in a cloud model. *J. Climate Appl. Meteor.*, **22**, 1065–1092.

List, R. and E.P. Lozowski, 1970: Pressure perturbations and buoyancy in convective clouds. *J. Atmos. Sci.*, **27**, 168–170.

Michalakes, J., S.-H. Chen, J. Dudhia, L. Hart, J. Klemp, J. Middlecoff, and W. Skamarock, 2001: Development of a next-generation regional weather research and forecast model. Mathematics and Computer Science Division, Argonne National Laboratory, ANL/MCS-P868-0101, 8pp.

Ogura, Y. and T. Takahashi, 1971: Numerical simulation of the life cycle of a thunderstorm cell. *Mon. Wea. Rev.*, **99**, 895–911.

Rutledge, S.A. and P.V. Hobbs, 1984: The mesoscale and microscale structure and organization of clouds and precipitation in midlatitude cyclones. XII: A diagnostic modeling study of precipitation development in narrow cold-frontal rainbands. *J. Atmos. Sci.*, **20**, 2949–2972.

Schlesinger, R.E., 1978: A three-dimensional numerical model of an isolated thunderstorm: Part I. Comparative experiments for variable ambient wind shear. *J. Atmos. Sci.*, **35**, 690–713.

Skamarock, W.C., J.B. Klemp, and J. Dudhia, 2001: Prototypes for the WRF (Weather Research and Forecast) model. Ninth Conf. Meso. Processes, AMS, J11–J15 (also see www.wrf-model.org).

Smagorinsky, J., 1963: General circulation experiments with the primitive equations. 1. The basic experiment. *Mon. Wea. Rev.*, **91**, 99–164.

Sun, W.Y., 1984: Numerical analysis for hydrostatic and nonhydrostatic equations of inertial-internal gravity waves. *Mon. Wea. Rev.*, **112**, 259–268.

———, W.Y. and J.D. Chern, 1993: Diurnal variation of lee-vortexes in Taiwan and surrounding area. *J. Atmos. Sci.*, **50**, 3404–3430.

———, W.Y. and P.A. Haines, 1996: Semi-prognostic tests of a new mesoscale cumulus parameterization scheme. *Tellus*, **48A**, 272–289.

Tao, W.K., J. Simpson, and M. McCumber, 1989: An ice-water saturation adjustment. *Mon. Wea. Rev.*, **117**, 231–235.

Yau, M.K., 1979: Perturbation pressure and cumulus convection. *J. Atmos. Sci.*, **36**, 690–694.

Wicker, L.J. and W.C. Skamarock, 1998: A time-splitting scheme for the elastic equations incorporating second-order Runge-Kutta time differencing. *Mon. Wea. Rev.*, **126**, 1992–1999.